Studying cancer cell migration under confinement and with correlative microscopy

Joana Marques Pinto Monteiro
joanampmonteiro@tecnico.ulisboa.pt

Instituto Superior Técnico, Lisboa, Portugal

November 2021

Abstract

Cancer cell migration is implicated in several clinically relevant phenomena, namely the formation of metastasis. It is then important to study the mechanisms involved in the migration of cancer cells, particularly in physiologically relevant 3D environments. In this work, we studied the migration of MDA-MB-231 breast cancer cells under confinement using polydimethylsiloxane (PDMS) devices comprising microconstrictions of different widths (2, 3 and 5 µm). Since Eps8L2 and Ctdnep1 were found to be involved in 2D cell migration, we investigated the role of these proteins in 3D cell migration. We calculated the duration of three nuclear transmigration periods – enter, cross and exit. We observed that nuclear deformation was necessary for confined cell migration, especially for narrower constrictions. However, we did not find an effect of constriction size in nuclear migration dynamics. Notably, the exit period of nuclear transmigration was, on average, shorter than the enter period for cells migrating across 2 and 3 µm-wide constrictions, but not 5 µm-wide constrictions. It was not possible to assess the role of Ctdnep1 and Eps8L2 in confined cell migration due to insufficient data. Moreover, we implemented a correlative microscopy workflow for the study of cell dynamics, consisting in phase-contrast live-cell imaging followed by fluorescence and super-resolution radial fluctuations (SRRF) imaging. Particularly, the NanoJ-Fluidics system was used to perform automatic staining of NIH 3T3 fibroblasts. Using this workflow, we successfully correlated cell dynamics with its underlying structural information. The strategies presented in this work can pave the way for further studies on cancer cell migration.

Keywords: cancer, cell migration, confinement, nuclear deformation, correlative microscopy

1. Introduction

Breast cancer is the most common malignancy in women [1], being the most prevalent type of cancer in the world [2]. Metastasis formation is the primary cause of death from cancer [2], in particular for the case of breast cancer, which has a high metastatic potential [3]. Since cancer cell migration is a key event in the formation of metastasis, the study of this topic is of high relevance in order to better understand the mechanisms involved in this process. Moreover, cancer cells encounter complex three-dimensional (3D) environments while migrating in enclosed spaces in the body, for example when passing across narrow openings, such as endothelial junctions for blood vessel intravasation and extravasation [4]. As such, it is particularly relevant to study cancer cell migration under confinement, through the use of appropriate systems recreating the complex 3D environments where migrating cancer cells can be found *in vivo*. Moreover, it is important to devise convenient approaches for the study of cell migration which enable the correlation of cell dynamics during migration and the structures that play a role in such dynamics. Applied to cancer, this can allow a better understanding of how certain phenomena involved in cell migration for the formation of mestastasis occur and what cellular elements are involved in the respective mechanisms.

2. Background

2.1. Mechanisms of 2D cell migration

The characteristics of cell migration, including the mode of migration, are influenced by several factors, such as the cell type and the physical and biochemical properties of the extracellular matrix (ECM) [5]. There are essentially two modes of two-dimensional (2D) single-cell migration: the mesenchymal and amoeboid modes [5, 6]. In mesenchymal migration, cells usually exhibit actin-rich protrusions, which can be the classic flat lamellipodia or thin elongated filopodia, and adhere strongly to the ECM through focal adhesions (mediated by integrins) by turn connected to the extremities of actomyosin stress fibers, resulting in slow migration speeds [5, 6]. On an-

other hand, amoeboid migration is characterized by rounded cell shapes, weak or no adhesion to the ECM and absence of mature focal adhesions and stress fibers, being much faster than the mesenchymal migration mode [5–7]. To migrate in this mode, cells either use actin-driven finger-like protrusions (pseudopods) or employ a contraction-based migration with the formation of blebs [5, 6, 8].

Nuclear positioning to the cell rear is important in cell migration for several cell types, such as mesenchymal cells, neurons, fibroblasts and most cancer cells [9]. Calero-Cuenca et al. (2021) found that Ctdnep1, a nuclear envelope phosphatase, and Eps8L2, an actin regulator, are involved in nuclear positioning for 2D fibroblast migration [10]. However, it is currently unknown whether these two proteins are also involved in 3D migration.

2.2. Mechanisms of 3D cell migration

As opposed to migration in a 2D environment, 3D migration is highly reliant on environmental factors, which can be divided into mechanical, chemical and geometrical [5, 11]. Moreover, cells are highly adaptive to their environment, employing and changing between a variety of migration modes in different contexts [5, 11]. Additionally to the mesenchymal and amoeboid modes of migration, cells can also employ a third mode of migration in 3D environments, conserving the subjacent fundamentals of force generation and transmission: a lobopodial type of migration, which can be seen as a hybrid between the mesenchymal and amoeboid migration modes [5, 11].

In general, there are two main mechanisms that cells employ to migrate through confined spaces: expanding the constriction by proteolytic degradation and/or physical remodeling of the ECM or alteration of cell shape and stiffness to fit in the gap [12, 13]. If a cell is migrating across a tight space that is narrower than the cell diameter, then its body adjusts its morphology accordingly [12]. Importantly, numerous studies have found that the ability of the nucleus to deform is the major limiting factor in migration through confined spaces [13–16]. Two of the main aspects determining the capacity of the nucleus to squeeze or deform are chromatin and the nuclear lamin network, particularly Lamin A/C [13, 17, 18].

There are at least three ways for cancer cells to migrate *in vivo*: gradual ECM degradation, migration through pre-existing gaps or tracks resembling channels and following cancer cells (or cancer-associated cells) that disclose passages for migration [19]. Cancer cells have a high capacity to migrate along tracks without the need for ECM degradation by employing an amoeboid migration mode, while also being able to employ, alternatively, a metalloproteinase (MMP)-dependent mesenchymal migration [19, 20]. Notably, unlike other cell types, cancer cells exhibit a high plasticity of migration mechanisms, being able to employ various migration modes depending on their surrounding 3D environment [19, 20]. This high plasticity may confer these cells with a unique ability to adapt to a wide range of environments, thus promoting disease progression [20]. Moreover, it has been shown that lamins are misregulated in many types of cancer, contributing to the ability of these cells to deform while migrating across confined spaces [13]. For example, lower levels of Lamin A/C expression have been reported in several types of cancer [13, 21]. This likely enhances the metastatic potential of these cells.

2.3. Platforms to study confined cell migration

The two main types of engineered 3D microenvironments for the study of confined cell migration are hydrogels recreating the ECM and microfabricated devices comprising microconstrictions [22]. These systems allow the study of different aspects of cell dynamics and structure, such as the ability of cells to migrate through very narrow spaces or to degrade fibers from ECM-like environments, and the changes in morphology exhibited by cells when placed under confinement [4]. Hydrogels can be mechanically tuned to study the effects of ligand density, substrate stiffness and pore size on cell migration [23]. This system has the advantage of allowing the formation of migration tracks similar to those found *in vivo* and, often unlike with microfabricated devices, with physiologically relevant stiffness [23]. However, the pores created in these gels are often smaller than the ones existing *in vivo*, in addition to the fact that it is not possible to control the track length and width as it is with other systems, such as microfabricated devices [23]. Microfabricated devices for the study of confined cell migration typically make use of polydimethylsiloxane (PDMS), given that this elastomer is optically transparent, thus allowing clear imaging of cells, biologically inert, and oxygen-permeable [23]. Due to their properties, these platforms allow for clear microscope time-lapse acquisitions and precise quantification of cell migration direction, velocity, and intracellular dynamics [22]. PDMS channels can mimic different types of structures found *in vivo* through which cancer cells migrate, such as bone cavities or the lumen of blood or lymphatic vessels [23].

2.4. Correlative microscopy for the study of cell migration

Correlative microscopy arises when two or more microscopy techniques are combined in a correla-

tive manner to analyze the same area in the sample, which can be performed simultaneously or sequentially, with the goal of retrieving the strengths of each technique, while downsizing their respective weaknesses [24]. For example, light microscopy can be correlated with super-resolution microscopy (SRM) or with electron microscopy, and variations of the same type of microscopy, such as phase contrast and fluorescence as sub-types of light microscopy, may also be correlated.

If the goal is to correlate cell dynamics with its underlying structural information, one can use NanoJ-Fluidics, a convenient approach developed in a collaboration between the Henriques and Leterrier laboratories [25], to perform live-to-fixed correlative imaging. This is an open-source, user-friendly system that allows automatic fluid exchange in microscopy experiments [25]. More specifically, it enables the performance of labeling and treatment protocols directly on the microscope stage in an automatic manner, which would otherwise have to be carried out at the bench, possibly interrupting microscope acquisitions [25]. Hence, by using this system, the same cells can be imaged in different conditions and with varying microscopy modalities, including SRM, which emphasizes how powerful this framework is for the performance of studies with correlative microscopy. This system makes use of LEGO®-based syringe pumps for fluid injection onto the sample and an Arduino® controller interface for automatic pump control [25]. The fact that the syringe pumps are built with LEGO® makes NanoJ-Fluidics an affordable and modular framework, allowing the execution of protocols in a repeatable and robust manner [25].

Although light microscopy alone can be used for live-to-fixed correlative imaging, its resolution is limited to approximately 300 nm due to light diffraction [24]. Thus, if the goal is to analyze certain cell structures in high detail, light microscopy could be correlated with SRM, which yields resolutions down to approximately 10-20 nm [24]. There is currently a wide variety of available SRM approaches, of which super-resolution radial fluctuations (SRRF) is an example [26]. To perform SRRF imaging, only the software is needed, thus making this a low cost SRM approach [26]. Additionally, it is capable of producing reconstructions of resolutions better than 150 nm even when the fluorescence signal emitted by the sample is low [26]. SRRF is a highly versatile technique, allowing to obtain both fixed-cell and dynamic live-cell super-resolution images with the use of conventional fluorophores, thus making it compatible with a wide range of imaging modalities [26]. In particular, it can be incorporated in experiments with NanoJ-Fluidics for the generation of super-resolution images from fixed-cell fluorescence images.

3. Materials and Methods

3.1. Cell culture

Highly-metastatic breast cancer MDA-MB-231 cells (herein referred to as MDA cells), a gift from Gonçalo Bernardes Lab (iMM), were cultured in Dulbecco Modified Eagle Medium (DMEM) with sodium pyruvate (11995065, Thermo Fisher Scientific), 10% fetal bovine serum (F0804-500ML, Merck) and penicillin-streptomycin (15140122, Thermo Fisher Scientific) at 120 units/ml. NIH 3T3 fibroblasts (CRL-1658, ATCC) were cultured in DMEM with no sodium pyruvate (41965039, Thermo Fisher Scientific), 10% bovine calf serum (35-053-CM, Corning), 10 mM HEPES (15630056, Thermo Fisher Scientific) and penicillin/streptomycin at 500 units/ml. Both cell lines were cultured at 37°C in 5% CO_2.

3.2. Production of MDA cell lines expressing NLS-GFP and LifeActin-mcherry

As the cell nucleus and actin filaments were structures of interest to observe in fluorescence microscopy experiments with the migration devices, MDA cells were infected with lentivirus expressing NLS-GFP and LifeActin-mcherry with puromycin resistance, produced in HEK293T cells (pLALI backbone). After changing the medium of cells at approximately 80% confluency in a 6-well plate, 10 µl of viral suspension for NLS-GFP expression were added to each well for half of the plate, and 10 µl of viral suspension for LifeActin-mcherry were added to each of the remaining wells. For selection of transfected cells, puromycin was added at 2.5 mg/ml for four days. To generate a double line, NLS-GFP-expressing cells were infected with lentiviral particles containing a plasmid for LifeActin-mcherry expression, following the same procedure. To obtain a cell line expressing both fluorescence genes for future use in experiments, fluorescence-activated cell sorting (FACS) was used.

3.3. siRNA transfection in MDA cells

To investigate the role of Ctdnep1 and Eps8L2 in confined cell migration, we recurred to siRNA to perform the knockdown of these proteins in MDA cells. The siRNAs that were used for cell transfection were Eps8L2 siRNA (HSS185565, Thermo Fisher Scientific), Ctdnep1 siRNA, which was custom made by GeneCust (sequence 5'-3': CAGCAUUGUGAUCCUGGAUTT), and the Silencer™ Select Negative Control No. 1 siRNA (4390843, Thermo Fisher Scientific), all at 20 µM concentration. MDA cells were transfected with each siRNA using Lipofectamine™ RNAiMAX Transfection Reagent (13778150, Thermo Fisher Scientific), by following the instructions provided by the manufacturer.

3.4. **Migration devices fabrication**

To produce the PDMS migration devices, we used molds already available in the lab, which were fabricated according to the design and procedure by Jan Lammerding Lab [27]. The migration devices were designed to include several features, including: two cell inlets through which cell seeding can be performed; sections with round micropillars that create constrictions 2 µm, 3 µm or 5 µm-wide through which the cells migrate; and two reservoirs for medium connected by a channel, used to create a chemotactic gradient to trigger cell migration in a given direction across the micropillars sections. The micropillar sections are 5 µm-tall and the areas in which the cells are seeded and gather after migration through the micropillars are 250 µm-tall.

PDMS was prepared using the SYLGARD™ 184 Silicone Elastomer Kit (Dow) by mixing the two components of the kit, elastomer base and curing agent, in the 10:1 ratio. The mixture was poured over the mold to make devices approximately 4 mm-thick and then degassed in a desiccator. PDMS was cured at 70°C for 1h and the resulting replica was carefully peeled away from the mold. Individual devices were cut out and the holes for the cell inlets and medium reservoirs were punched with 1.2 mm and 5 mm biopsy punches, respectively.

To assemble the final microfluidic devices the PDMS replicas were bonded to microscope glass slides. Glass slides were immersed in Alconox® Powdered Precision Cleaner (1104-1, Alconox) at 10 g/L and cleaned in an ultrasonic bath at 70°C for 1 hour and 30 minutes. Both the PDMS devices and the glass slides were then thoroughly washed with ethanol 70% followed by deionized water and left in a laminar flow hood to dry. For the bonding, the glass slides and the devices were submitted to ultraviolet/ozone treatment for 5 minutes, and the PDMS devices were placed on the glass slides.

3.5. **Preparation of devices and cell seeding**

Two days after transfection with siRNA, the devices were prepared and cell seeding was performed, based on a protocol described elsewhere [28]. Briefly, the medium reservoirs of the devices were washed once with ethanol 70%, then washed three times with deionized water and finally washed with phosphate-buffered saline (PBS, 18912014, Thermo Fisher Scientific). To enhance cell attachment and migration, human fibronectin (356008, Corning) at 20 µg/ml in PBS was added to all reservoirs of the devices. The devices were incubated at 37°C for 1h. After removing the coating solution from the devices, the medium reservoirs were washed with of PBS and filled with medium, which was removed right before cell seeding. Cells were resuspended in appropriate volume of medium and 5 µl of the suspension were carefully pipetted into the cell inlet closest to the edge of the device for each condition. Upon observation under the microscope, the medium reservoirs in the opposite side of the cells were filled with medium.

3.6. **Preparation of devices for microscopy**

The preparation of the devices for imaging was performed one day after cell seeding, right before microscope imaging. Medium in the devices was aspirated slowly with a pipette and the medium reservoirs were carefully washed with PBS. Hepatocyte growth factor (HGF) human recombinant (100-39B, tebu-bio) mixed in medium at the 1:10 ratio was added to the reservoir in the opposite side of the cells, and medium was added to the reservoir in the same side of the cells, at the same time, to establish a chemotactic gradient. Two glass cover slips were used to cover the two devices to minimize medium evaporation during the experiment.

3.7. **Imaging of cells in migration devices**

The glass slide with the devices was placed in a widefield microscope stage inside a temperature-controlled incubator pre-heated at 37°C and with 5% CO_2 supply. Positions for image acquisition were chosen and the system was left to stabilize temperature-wise before starting image acquisition. Widefield images were acquired with a 20x objective every 10 minutes for an overnight period between 12 and 18 hours total. A Z-stack of either 3 or 5 slices (centered in the focal plane) within a range of 4.24 µm was acquired for every position. Bright-field images, as well as red and green fluorescence images using LED lights of 561 nm and 488 nm, respectfully, were acquired.

3.8. **Analysis of images from cell migration in PDMS devices**

We only analyzed cells that appeared healthy, did not divide or result from cell division at a critical time point for migration through the constrictions, with no adjoining dead or live cells that could affect the migration dynamics, and passing through undamaged micropillars. Prior to cell migration quantification, image stacks were selected and aligned in FIJI (ImageJ).

For quantification of cell migration through the constrictions, a rectangle with approximately 10 µm of width was drawn in FIJI in the center of the micropillars through which the cell passed. Four key time points in the migration of the cell through the micropillars were considered: the time point at which the cell nucleus first reaches the left side of the rectangle ($t1$), which is considered to be 0 for simplification, the time point at which the nucleus first reaches the right side of the rectangle ($t2$), the time point at which the nucleus first passes through

the left side of the rectangle ($t3$) and the time point at which the nucleus first passes through the right side of the rectangle ($t4$). The time that passed between each of these time points was then calculated for each cell, namely $t2 - t1$, denoted as enter period, $t3 - t2$, denoted as cross period, $t4 - t3$, denoted as exit period, and $t4 - t1$, denoted as transit period. Different plots of these periods were then produced for comparison between siRNA transfection conditions and constriction sizes. Additionally, the width of the constriction through which each cell migrated was measured in FIJI. Plots were produced in GraphPad Prism 8.

3.9. **Statistical analysis**

Groups for which there was sufficient migration quantification data were tested for significant difference among means using an ordinary one-way ANOVA test. Tukey's multiple comparisons test was also employed to assess which were the groups whose means were significantly different among themselves. A p-value of less than 0.05 was considered significant. Statistical analysis was performed with GraphPad Prism 8.

3.10. **Assembly of pumps for correlative microscopy with NanoJ-Fluidics**

The NanoJ-Fluidics system makes use of LEGO®-based syringe pumps to automate fluid exchange procedures in microscopy. The various components of NanoJ-Fluidics were assembled and installed according to the available wiki made by the authors [29]. A 3D-printed version of the pumps was assembled to use for the microscopy experiments as it would confer increased stability to the construct when compared to the original LEGO® pumps. The 3D-printed structures used to assemble the pumps in the present work were kindly provided by Ricardo Henriques (IGC), from the designs of Matthew Meyer (The Ohio State University, OSU), which can be found in the wiki [30–32]. One fully built pump making use of 3D-printed structures was gifted by Pedro Pereira (ITQB). A custom-made stand for the pumps and electronics hardware was made using regular LEGO® pieces and DUPLO® pieces. An image of the assembled pump set-up can be seen in Figure 1.

3.11. **Live imaging of NIH 3T3 fibroblasts**

The microscope used for live and fixed imaging of NIH 3T3 fibroblasts for correlative microscopy was Nikon Eclipse Ti. A 35-mm glass-bottomed dish (81158, ibidi) containing cells at approximately 20% confluency was placed under the microscope in a small stage temperature-controlled incubator preheated at 37°C and with 5% CO_2 supply. The sample was covered with the lid comprising holes for the tubing and the tubing was connected to the sample,

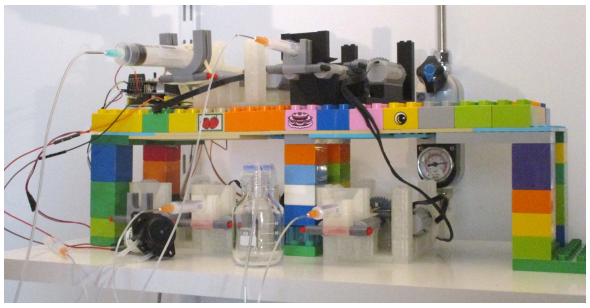

Figure 1: Pump set-up that was used for cell staining procedures with NanoJ-Fluidics, which includes the custom-made pump stand, the syringe pumps and peristaltic pump with respective labware, the electronics hardware, and a glass container for liquid waste.

making sure that the dish was stable in the incubator to avoid its misplacement. The live imaging sequence consisted in the acquisition of widefield phase contrast images in several positions of the sample with a 60x objective in oil immersion every 60 seconds for a total period of 30 minutes. A Z-stack of 9 slices (centered in the focal plane) with a 0.5 µm step was acquired for every position and he Perfect Focus System was used. The image stacks resulting from live-cell imaging sequences were selected and aligned in FIJI.

3.12. **Staining protocol used for experiments with NanoJ-Fluidics**

In this work, NIH 3T3 fibroblasts were stained for vinculin, phalloidin and DAPI. The final cell staining procedure that was used in the experiments with NanoJ-Fluidics is described here. After medium aspiration, cells in 35-mm glass-bottomed dishes at approximately 20% confluency were fixed with 2 ml of 4% paraformaldehyde (PFA) in PBS, prepared from a 16% PFA aqueous solution (E15711, Science Services), which was left in the dish for 10 minutes. Cells were washed five times with 1 ml of PBS for 2 minutes and then permeabilized with 1 ml of Triton™ X-100 (X100-1L, Merck) diluted at 0.5% in PBS for 5 minutes, followed by another three 1 ml PBS washes of 5 minutes each. A volume of 500 µl of mouse monoclonal anti-vinculin antibody (V9264-200UL, Merck) diluted at 1:200 in 10% goat serum (G9023-10ML, Merck) in PBS was added to the cells and left in the dish for 30 minutes, after which cells were washed three times with 1 ml of PBS for 5 minutes. A volume of 500 µl of DAPI (32670-5MG-F, Merck) and Alexa Fluor® 488 Phalloidin (A12379, Thermo Fisher Scientific) diluted at 1:100 and Alexa Fluor® 555 goat anti-mouse IgG (H+L) highly cross-adsorbed secondary antibody (A-21424, Thermo Fisher Scientific) diluted at 1:600 in 10% goat serum in PBS was added to the cells and left in the dish for 30 minutes. Cells were washed three times with 1 ml of PBS for 5

minutes and left covered in 1 ml of PBS.

A sequential protocol was created in order to allow the performance of an automatic cell staining procedure using the pumps. All steps described above were included in the automated protocol except for the fixation step, as the fixative was injected manually. In short, immediately after the time-lapse acquisition of cells ended, the medium was aspirated using the peristaltic pump and the fixative was manually injected right after. 10 minutes after injecting the fixative, the sequential protocol was started. The goal of proceeding in this manner was to allow the performance of correlative microscopy, meaning that the last frame of the time-lapse of a given cell could be accurately correlated with an image of several stained structures of the same cell.

3.13. **Fluorescence imaging of fixed cells**

Fixed-cell imaging consisted in the acquisition of widefield phase contrast and fluorescence images with a 60x objective in oil immersion in the selected positions. A Z-stack of 11 slices (centered in the same focal plane as for the time-lapse acquisition) with a 0.5 µm step was acquired for every position. Fluorescence images were acquired using the Intensilight Hg Pre-Centered Fiber Illuminator (Nikon) exciting the sample either in the 528-553 nm, 465-495 nm or 340-380 nm ranges to obtain either red, green or blue fluorescence images, respectively.

3.14. **SRRF imaging of fixed cells**

With the goal of obtaining images containing cellular structures with more definition than that achieved with widefield fluorescence imaging, SRRF images were produced in FIJI using the plugin "Nano-J SRRF" and choosing "SRRF Analysis". For each fluorescence channel of interest, namely red for vinculin and green for actin, 100 fluorescence images of a cell of interest were given as input and the default parameters of the software were used, as they were found to be optimal for image quality overall. To compare the sharpness of the structures obtained with SRRF with that of the widefield fluorescence images, the intensity profiles of pixels sitting in a small line drawn perpendicularly to actin filaments were traced in FIJI, for both types of images of an example cell.

4. Results and Discussion

4.1. **MDA cell migration through microconstrictions**

Given the occurrence of technical problems throughout the experiments, we did not perform any analysis on the dynamics of actin filaments, and therefore only analyzed nuclear dynamics using NLS-GFP-expressing MDA cells. A representative time-lapse image of an MDA cell migrating through a 3 µm-wide constriction can be seen in Figure 2. As exemplified in Figure 2, cells migrated through the constrictions formed by micropillars according to a chemotactic gradient of HGF, as it was expected. Cells, most noticeably the nuclei, underwent deformation to fit into the constrictions of several dimensions, having deformed more significantly for narrower constrictions. These highly pronounced changes in the shape of the nucleus have been observed *in vivo* during cancer cell spreading [33] and diapedesis [34].

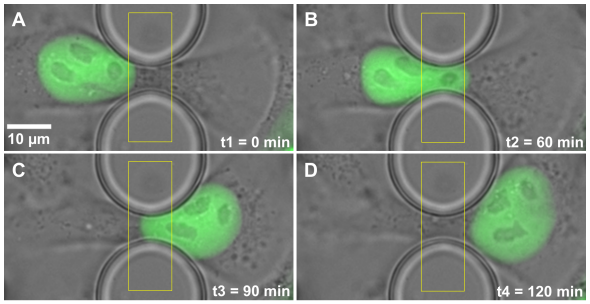

Figure 2: Selected frames from a widefield microscopy (brightfield and fluorescence images overlapped) time-lapse recording of a cell transfected with Ctdnep1 siRNA migrating through a PDMS constriction with 3 µm of width, in which the cell nucleus is marked with NLS-GFP. The four selected frames (A, B C and D) represent the frames at which the time points $t1$, $t2$, $t3$ and $t4$ were measured, respectively.

4.2. **Measurement of constriction widths**

In order to assess how similar the constriction widths of the microdevices were when compared to the widths of the original device design, namely 2 µm, 3 µm and 5 µm, the distances between round micropillars for all cells that were quantified were measured. A plot containing all the measurements made for each constriction width category is presented in Figure 3. It can be observed that the means of the distances measured between round micropillars are higher than the expected values, for all constriction types, additionally to being highly variable in each group. This could be a consequence of the conditions of the mold that was used for the fabrication of the devices and of a shrinkage effect that cured PDMS can experience, which does not always occur to the same extent [35–37].

4.3. **Effect of constriction size in nuclear migration periods**

The duration of each nuclear migration period for the cells transfected with control siRNA that were analyzed was plotted for the three constriction widths, to assess if the constriction size had an effect on the duration of the migration periods (see Figure 4). It can be observed that no statistically significant difference among means of each period duration for different constriction sizes could be found. This data suggests that constriction size

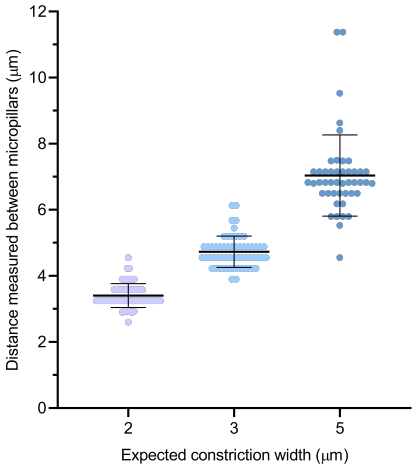

Figure 3: Distances measured between round micropillars for all cells whose nuclear migration dynamics were quantified, for each constriction width category (2 µm, 3 µm and 5 µm). For each column, the mean and standard deviation of the data are represented with black lines. n = 57, 58 or 46 cells for the 2, 3 or 5 µm-wide constrictions cell group, respectfully.

does not influence the velocity of nuclear migration under confinement. However, it was found that there was high variability among measured constriction widths (see Figure 3), which might hamper the drawing of conclusions about the effect of constriction size on the nuclear migration dynamics of cells.

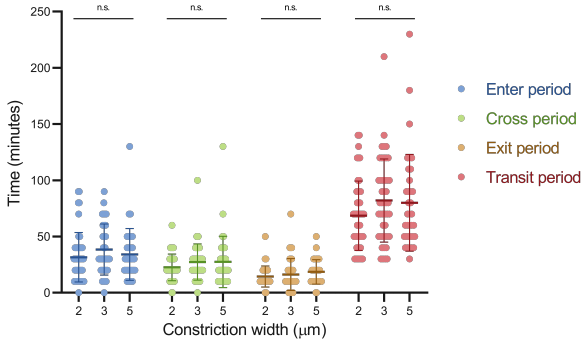

Figure 4: Duration of each nuclear migration period for different constriction widths in NLS-GFP-expressing MDA cells transfected with control siRNA. For each column, the mean and standard deviation of the data are represented with darker-colored lines. n = 46, 45 or 35 cells for the 2, 3 or 5 µm-wide constrictions cell group, respectfully. n.s., non-significant, $p > 0.05$ (ANOVA test).

Several authors who studied confined cell migration using microfabricated devices have found that, for constriction widths in a similar range, the narrower the constriction, the slower the cells migrated across the constriction [14, 38–40]. This was found for several cell types, including MDA-MB-231. Thus, it would have been plausible to find a statistically significant difference between groups of nuclear migration periods for different constriction widths in the present work. An explanation for this not being the case could be, as mentioned before, the disparities among constriction widths for each type of constrictions and overlapping of constriction sizes for different categories.

4.4. Differences between nuclear migration periods

In order to analyze the data from cells transfected with control siRNA on another perspective, the duration of the several nuclear migration periods was plotted for each constriction width, to study how nuclear migration periods are different from one another (see Figure 5). It can be observed that the means of the enter and exit periods were significantly different from one another for the 2 and 3 µm-wide constriction cell groups. Together with the visual representation of the data in the plot, this suggests that the exit period is shorter than the enter period for constrictions of smaller widths. For the 5 µm-wide constriction cell groups, however, these two periods do not seem to be significantly different. A way to interpret these findings is by having in mind that, the wider the constriction, the closer the conditions are to a 2D environment. Therefore, it might be logical that there are different mechanisms of nuclear compression and relaxation for narrower constrictions and not for wider constrictions, as the latter do not affect the entry and exit of the nucleus as much.

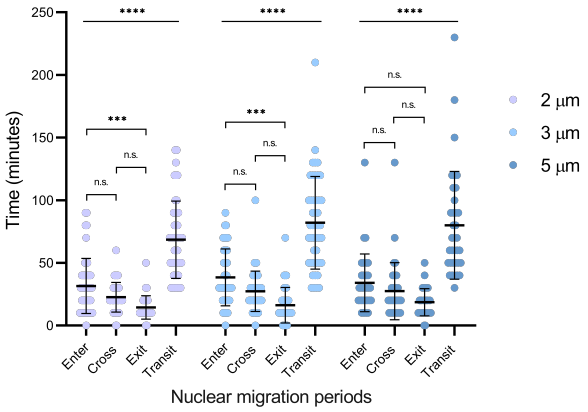

Figure 5: Duration of all nuclear migration periods for each constriction width in NLS-GFP-expressing MDA cells transfected with control siRNA. For each column, the mean and standard deviation of the data are represented with black lines. n = 46, 45 or 35 cells for the 2, 3 or 5 µm-wide constrictions cell group, respectfully. ****, p < 0.0001 (ANOVA test). n.s., non-significant, $p > 0.05$; ***, $p = 0.005$ for the 2 µm group and $p = 0.001$ for the 3 µm group (Tukey's multiple comparisons test).

Regarding the finding that the enter period is larger than the exit period for cells migrating through narrower constrictions, there are several studies with various cell types, including cancer

cells, that obtained similar results [13,27,41]. These findings seem to be in line with the notion that the deformation of the nucleus is the rate-limiting step during confined migration. Moreover, these results could indicate that there are different mechanisms for nuclear compression and nuclear relaxation. Because nuclear squeezing or deformation is necessary for its entry into a constriction, chromatin condensation and Lamin A/C expression levels seem to be particularly relevant for nuclear compression in the enter period. On the other hand, the mechanism driving fast nuclear relaxation in the exit period might be partially explained by a release of elastic energy that had been stored due to significant nuclear deformation [41, 42].

4.5. Effect of siRNA transfection in MDA cells for confined nuclear migration

We were not able to obtain sufficient quantification data from confined nuclear migration of cells transfected with Eps8L2 and Ctdnep1 siRNA, particularly when compared to the data obtained for cells transfected with control siRNA. Therefore, we chose not to analyze or present the data referent to cells transfected with Eps8L2 and Ctdnep1 siRNA.

4.6. Widefield images from correlative microscopy experiments

The staining procedure was performed successfully with NanoJ-Fluidics using the defined sequential protocol. When doing live imaging of cells, it was noticed that there were cells which were more static and did not seem to migrate, and there were cells which, on the other hand, were more dynamic and migrated during the 30-minute acquisition period. For this reason, it seemed interesting to compare the structures of these cells after the staining procedure. Widefield images from "static" and "dynamic" cells in the sample before and after the staining procedure with NanoJ-Fluidics can be seen in Figure 6.

When viewing the staining images from both cells (see Figure 6D,F), it is possible to conclude that the last frame from live imaging was correctly correlated with an image containing all fluorescence channels from the cell staining overlapped. Regarding differences between the fluorescence images from the two cells, which include staining for vinculin, present in focal adhesions, actin filaments and the nucleus, Figure 6D shows that the "static" cell had a high amount of actin stress fibers with focal adhesions in their extremities, while Figure 6F shows that the "dynamic" cell did not have these structures, showing less defined actin filaments instead and less localized vinculin. These observations suggest that the top cell depicted in Figure 6A could be migrating in a mesenchymal mode, while the cell in Figure 6B could be migrating in an amoeboid mode, given the key differences between these two modes of migration. The fact that the top cell in Figure 6A, claimed to be employing a mesenchymal mode of migration, seemed to be static throughout the 30 minute-long time-lapse, might be due to the fact that the live-cell acquisition was not long enough capture cell displacement in this rather slow mode of migration. Thus, using NanoJ-Fluidics, it was possible to correlate live and fixed-cell imaging to observe the details of certain cell structures in cells with different types of dynamics.

4.7. SRRF imaging of fixed cells

It was possible to generate SRRF images from the cells shown in Figure 6 with relatively good quality (images not shown here). In particular, it was possible to infer that the SRRF images were able to provide a sharper visualization of the stained structures, especially actin filaments, when compared to their corresponding widefield fluorescence images. Pixel intensity profiles were traced for the cell shown in Figure 6D and showed that the SRRF image resolved better the actin filaments than the widefield fluorescence image. In particular, the pixel intensity profile of an actin filament in the SRRF image exhibited a narrow, well-defined peak, whereas that of the widefield fluorescence image exhibited a much wider, less-defined peak. Thus, it was possible to correlate super-resolution images of structural information of the cell with its dynamics observable in live imaging using NanoJ-Fluidics.

5. Concluding Remarks

With this work, it was possible to study cancer cell migration under confinement, as well as successfully implement a correlative microscopy workflow for the correlation of cell dynamics with its underlying structural information. Regarding the experiments with microfabricated devices, we could observe the nuclear squeezing behavior that is typically observed in cells migrating across narrow spaces and found that the enter period of nuclear transmigration was, on average, higher than the exit period for cells migrating across narrower constrictions. Concerning the correlative microscopy experiments, the NanoJ-Fluidics system showed to be a powerful tool for bridging the gap in the complex task of performing live and fixed imaging on the same cells. Additionally, we were able to generate SRRF images, which further showcases the applicability of this system.

Future work in the line of this study may include the repetition of the same workflow for the study of confined cancer cell migration with the goal of obtaining more data to investigate actin filaments dynamics and the role of Ctdnep1 and Eps8L2 in confined cell migration. Moreover, better control over the device microstructures should be ensured

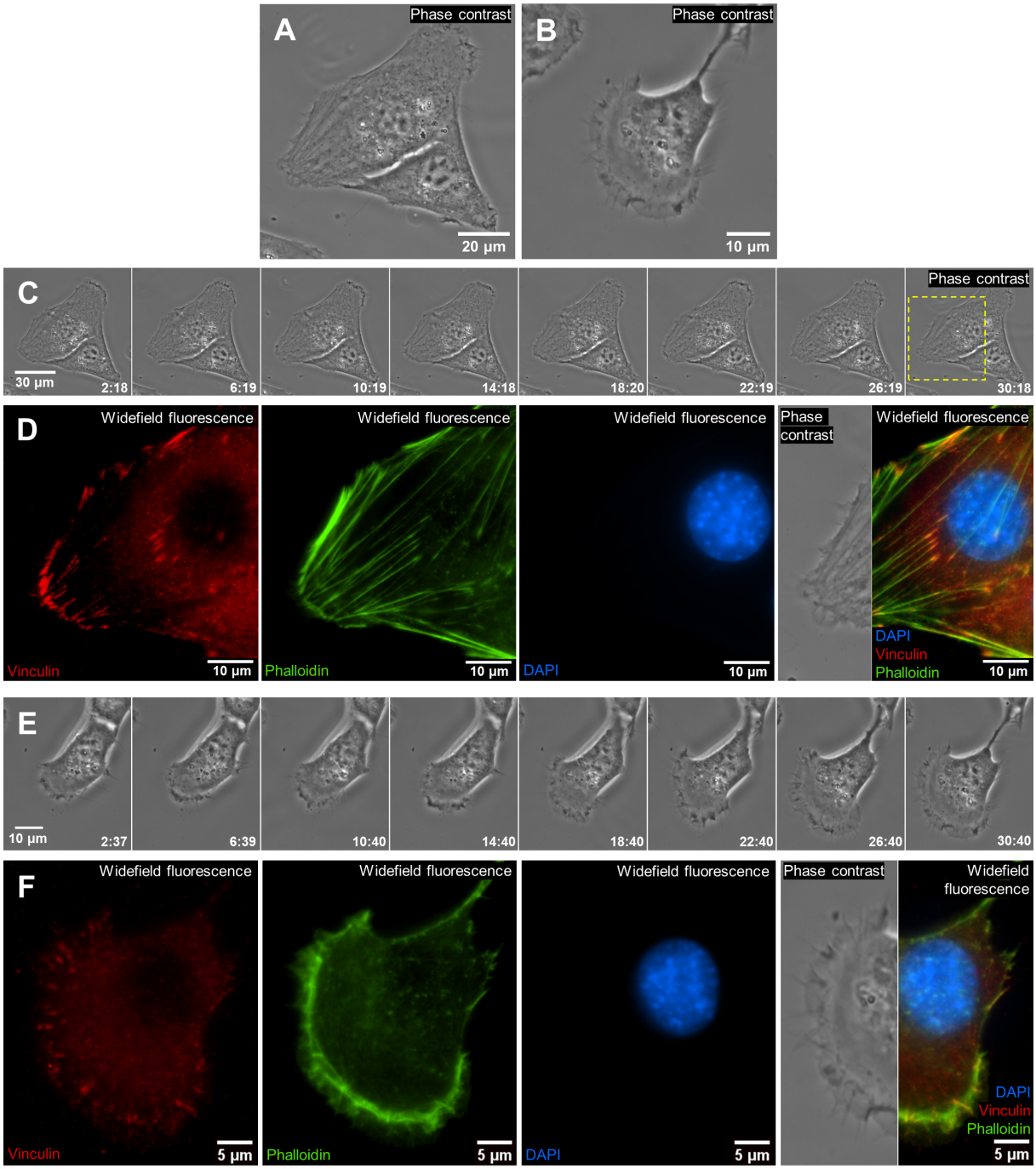

Figure 6: **Widefield images of cells in the sample obtained before and after performing a staining procedure using NanoJ-Fluidics.** (A) and (B) Widefield phase contrast images from "static" (A) and "dynamic" (B) cells in the sample immediately before fixation. (C) and (E) Frames from time-lapse recordings of the cells represented in (A) and (B), respectfully, where the last frame is the last image acquired right before fixation, for each cell. (D) and (F) Widefield fluorescence images of the cells represented in (A) and (B), respectfully, acquired after the staining procedure (in (D) it is the selected region indicated by the yellow rectangle in (C)). From left to right: vinculin staining (red), actin staining with phalloidin (green), nucleus staining with DAPI (blue), and a portion from the last frame of the time-lapse next to a fluorescence image of the three staining images overlapped. For each cell, the image of the DAPI staining is from a different focal plane than that of the remaining staining images, in order to allow a good visualization of all stained structures.

for the obtainment of more reliable results. Furthermore, the two workflows implemented in this work could be combined in order to expand the possibilities for the study of cancer cell migration.

The platforms and workflows here presented for the study of cancer cell migration can contribute to a better understanding of the phenomena involved in cancer cell migration for metastization as well as

other clinically relevant events, not being restricted to cancer. The work here developed can then pave the way for studies with higher clinical relevance, namely drug development and investigation of preventive measures for metastasis formation.

Acknowledgements

This document was written and made publically available as an institutional academic requirement and as a part of the evaluation of the MSc thesis in Biomedical Engineering of the author at Instituto Superior Técnico. The work described herein was performed at the Edgar Gomes Lab of Instituto de Medicina Molecular João Lobo Antunes, Faculty of Medicine of the University of Lisbon (Lisboa, Portugal), during the period March-October 2021, under the supervision of Dr. Edgar Gomes and Dr. Francisco Calero-Cuenca. The thesis was co-supervised at Instituto Superior Técnico by Professor Gabriel Monteiro.

References

[1] N. Pasha and N. C. Turner. Understanding and overcoming tumor heterogeneity in metastatic breast cancer treatment. *Nature Cancer*, 2:680–692, 2021.

[2] WHO. Cancer, 2021. URL `https://www.who.int/en/news-room/fact-sheets/detail/cancer`. Online; accessed October 2021.

[3] Y.-H. V. Ma, K. Middleton, et al. A review of microfluidic approaches for investigating cancer extravasation during metastasis. *Microsystems & Nanoengineering*, 4:17104, 2018.

[4] M. Mak, C. Reinhart-King, et al. Elucidating mechanical transition effects of invading cancer cells with a subnucleus-scaled microfluidic serial dimensional modulation device. *Lab on a chip*, 13(3):340–348, 2013.

[5] S. Seetharaman and S. Etienne-Manneville. Cytoskeletal Crosstalk in Cell Migration. *Trends in Cell Biology*, 30(9):720–735, 2020.

[6] D. G. Blackley, J. H. Cooper, et al. Mechanics of developmental migration. *Seminars in Cell & Developmental Biology*, 2021.

[7] P. O'Neill, J. Castillo-Badillo, et al. Membrane Flow Drives an Adhesion-Independent Amoeboid Cell Migration Mode. *Developmental Cell*, 46(1):9–22.e4, 2018.

[8] B. Alvarez-González, R. Me, et al. Cytoskeletal Mechanics Regulating Amoeboid Cell Locomotion. *Applied mechanics reviews*, 66(5):0508041–05080414, 2014.

[9] F. J. Calero-Cuenca, C. S. Janota, et al. Dealing with the nucleus during cell migration. *Current Opinion in Cell Biology*, 50:35–41, 2018.

[10] F. J. Calero-Cuenca, D. S. Osorio, et al. Ctdnep1 and Eps8L2 regulate dorsal actin cables for nuclear positioning during cell migration. *Current Biology*, 31(7):1521–1530.e8, 2021.

[11] K. Yamada and M. Sixt. Mechanisms of 3D cell migration. *Nature Reviews Molecular Cell Biology*, 20(12):1–15, 2019.

[12] L. Liu, Q. Luo, et al. Nucleus and nucleus-cytoskeleton connections in 3D cell migration. *Experimental Cell Research*, 348(1):56–65, 2016.

[13] A. L. McGregor, C.-R. Hsia, et al. Squish and squeeze—the nucleus as a physical barrier during migration in confined environments. *Current Opinion in Cell Biology*, 40:32–40, 2016.

[14] Y. Fu, L. K. Chin, et al. Nuclear deformation during breast cancer cell transmigration. *Lab on a chip*, 12:3774–8, 2012.

[15] K. Wolf, M. te Lindert, et al. Physical limits of cell migration: Control by ECM space and nuclear deformation and tuning by proteolysis and traction force. *Journal of Cell Biology*, 201(7):1069–1084, 2013.

[16] P. Davidson, C. Denais, et al. Nuclear deformability constitutes a rate-limiting step during cell migration in 3-D environments. *Cellular and Molecular Bioengineering*, 7(3):293–306, 2014.

[17] M. Doolin, R. Moriarty, et al. Mechanosensing of Mechanical Confinement by Mesenchymal-Like Cells. *Frontiers in physiology*, 11:365, 2020.

[18] X. Cao, E. Moeendarbary, et al. A Chemomechanical Model for Nuclear Morphology and Stresses during Cell Transendothelial Migration. *Biophysical Journal*, 111(7):1541–52, 2016.

[19] C. Paul, P. Mistriotis, et al. Cancer cell motility: lessons from migration in confined spaces. *Nature Reviews Cancer*, 17:131–140, 2016.

[20] S. SenGupta, C. Parent, et al. The principles of directed cell migration. *Nature Reviews Molecular Cell Biology*, 22(8):529–547, 2021.

[21] C. Capo-Chichi, K. Cai, et al. Loss of A-type lamin expression compromises nuclear envelope integrity in breast cancer. *Chinese journal of cancer*, 30(6):415–25, 2011.

[22] N. Zuela-Sopilniak and J. Lammerding. Engineering approaches to studying cancer cell migration in three-dimensional environments. *Philosophical Transactions of the Royal Society B: Biological Sciences*, 374(1779):20180219, 2019.

[23] C. D. Paul, W.-C. Hung, et al. Engineered Models of Confined Cell Migration. *Annual Review of Biomedical Engineering*, 18(1):159–180, 2016.

[24] M. Hauser, M. Wojcik, et al. Correlative Super-Resolution Microscopy: New Dimensions and New Opportunities. *Chemical Reviews*, 117(11):7428–7456, 2017.

[25] P. Almada, P. Pereira, et al. Automating multimodal microscopy with NanoJ-Fluidics. *Nature Communications*, 10(1):1223, 2019.

[26] N. Gustafsson, S. Culley, et al. Fast live-cell conventional fluorophore nanoscopy with ImageJ through super-resolution radial fluctuations. *Nature Communications*, 7(1):12471, 2016.

[27] P. M. Davidson, J. Sliz, et al. Design of a microfluidic device to quantify dynamic intra-nuclear deformation during cell migration through confining environments. *Integrative Biology*, 7(12):1534–1546, 2015.

[28] J. Keys, A. Windsor, et al. *Assembly and Use of a Microfluidic Device to Study Cell Migration in Confined Environments: Methods and Protocols*, volume 1840, pages 101–118. 2018.

[29] NanoJ-Fluidics: open-source fluid exchange in microscopy, 2019. URL `https://github.com/HenriquesLab/NanoJ-Fluidics/wiki`. Online; accessed October 2021.

[30] MMeyer_SolidPumpy_2_5.stl, 2019. URL `https://bit.ly/3BI0cuo`. Online; accessed October 2021.

[31] MMeyer_Pumpy_BD60ml_2_5.stl, 2019. URL `https://bit.ly/3BJadHT`. Online; accessed October 2021.

[32] MMeyer_Pumpy_BD3ml_2_5.stl, 2019. URL `https://bit.ly/3lFdIt8`. Online; accessed October 2021.

[33] S. Alexander, G. E. Koehl, et al. Dynamic imaging of cancer growth and invasion: a modified skin-fold chamber model. *Histochemistry and cell biology*, 130(6):1147–54, 2008.

[34] m.-B. Voisin, A. Woodfin, et al. Monocytes and Neutrophils Exhibit Both Distinct and Common Mechanisms in Penetrating the Vascular Basement Membrane In Vivo. *Arteriosclerosis, thrombosis, and vascular biology*, 29(8):1193–9, 2009.

[35] M. Madsen, N. Feidenhans'l, et al. Accounting for PDMS shrinkage when replicating structures. *Journal of Micromechanics and Microengineering*, 24(12):127002, 2014.

[36] D. B. Wolfe, J. C. Love, et al. *Nanostructures Replicated by Polymer Molding*, pages 2657–66. Marcel Dekker, Inc., New York, 2004. 893.

[37] C. Moraes, Y. Sun, et al. Solving the shrinkage-induced PDMS alignment registration issue in multilayer soft lithography. *Journal of Micromechanics and Microengineering*, 19(6):065015, 2009.

[38] D. Irimia and M. Toner. Spontaneous migration of cancer cells under conditions of mechanical confinement. *Integrative biology: quantitative biosciences from nano to macro*, 1(8-9):506–12, 2009.

[39] B. Nath, A. P. Bidkar, et al. Deciphering Hydrodynamic and Drug-Resistant Behaviors of Metastatic EMT Breast Cancer Cells Moving in a Constricted Microcapillary. *Journal of Clinical Medicine*, 8(8), 2019.

[40] Z. Tong, E. M. Balzer, et al. Chemotaxis of Cell Populations through Confined Spaces at Single-Cell Resolution. *PLOS ONE*, 7(1):1–10, 2012.

[41] M. Krause, F. W. Yang, et al. Cell migration through three-dimensional confining pores: speed accelerations by deformation and recoil of the nucleus. *Philosophical Transactions of the Royal Society B: Biological Sciences*, 374(1779):20180225, 2019.

[42] L. Lautscham, C. Kämmerer, et al. Migration in Confined 3D Environments Is Determined by a Combination of Adhesiveness, Nuclear Volume, Contractility, and Cell Stiffness. *Biophysical Journal*, 109:900–13, 2015.